Comprehensive Char Particle Gasification Model Adequate for Entrained-Flow and Fluidized-Bed Gasifiers

Matthew B. Tilghman,[†] Nils Erland L. Haugen,[‡] and Reginald E. Mitchell*,[†]

[†]High Temperature Gasdynamics Laboratory, Mechanical Engineering Department, Stanford University, Stanford, California 94305, United States

[‡]SINTEF Energy Research, 7465 Trondheim, Norway

ABSTRACT: A robust, single-particle gasification model is presented that is capable of predicting char particle behavior in environments established in typical fluidized-bed and entrained-flow gasifiers. It employs a heterogeneous reaction mechanism that describes char reactivity to CO_2, H_2O, and O_2 in the presence of H_2 and CO, gases that inhibit char reactivity. An effectiveness factor—Thiele modulus ($\eta-\varphi$) approach is used to determine overall conversion rates when species concentration gradients exist inside particles, which occur at high particle temperatures when chemical reaction rates and mass transport rates through particle pores become competitive. In the approach taken, a $\eta-\varphi$ relation is determined for each reactive gas (CO_2, H_2O, and O_2) and deviations from first-order behavior are correlated with the concentrations of the inhibitors (CO and H_2). A mean effectiveness factor is defined on the basis of the individual species effectiveness factors and used in a mode of conversion model that governs the variations in particle size and apparent density during char conversion. In this paper, the pertinent model equations are presented, with focus on the effectiveness factor—Thiele moduli relations. The model is shown to be useful in identifying rate-limiting processes during char conversion in gaseous environments varying in temperature and composition. It serves as a tool that can be used to help design efficient coal- and biomass-fired entrained-flow and fluidized-bed gasifiers as well as combustors.

1. INTRODUCTION

Kinetic parameters that describe intrinsic char reactivity are usually derived under conditions where mass transport effects are insignificant, so that variations in char mass loss rates can be attributed solely to the effects of chemical reactions.[1−8] Such conditions occur at low temperatures, where the rates of mass transport via diffusion through particle pores are fast compared to chemical reaction rates. When conversion rates are limited by reaction rates alone, mass diffusion time scales are much shorter than chemical reaction time scales, and therefore, the reactive gases completely penetrate the particles; concentrations inside particles are uniform at the levels existing at the outer surfaces of particles. At higher temperatures, kinetic and diffusion time scales become more similar, and as a result, gradients in the reactive gas concentrations are established inside particles. This causes the conversion rates inside particles to vary with the radius, with the conversion rates being highest near the peripheries of particles where the reactive gas concentrations are highest.

Concentration gradients can also develop inside particles under conditions when gasification rates are inhibited by H_2 and CO. The concentrations of these species can vary within the particle as a result of the competition between the chemical reactions that produce and consume these species and their rates of diffusion through particle pores. Account must be made for the combined effects of the chemical reaction and mass transport of both the reactive gases and the gases that inhibit reaction rates to accurately predict char particle mass loss rates during gasification. With a detailed heterogeneous reaction mechanism, accounting for the combined effects requires a direct numerical simulation (DNS) of the char conversion process employing a model that describes the effects of species diffusion through particle pores with the chemical reaction along pore walls. We have developed such a DNS code, which uses a heterogeneous reaction mechanism that describes the intrinsic chemical reactivity of char to O_2 and accounts for both Knudsen and bulk diffusion of oxygen through randomly oriented particle pores and for Stefan flow.[9] Since this initial work, the DNS code has been modified to include a heterogeneous reaction mechanism that describes char reactivity to O_2, CO_2, and H_2O to permit its use in steam gasification environments. The global, overall reactions that the mechanism kinetically describes are $C + H_2O \Leftrightarrow CO + H_2$, $C + CO_2 \Leftrightarrow 2CO$, and $C + (1 − \alpha/2)O_2 \Leftrightarrow \alpha CO + (1 − \alpha)CO_2$, where α depends upon the temperature.

In this paper, we use the results of DNS using the modified code to derive effectiveness factors, defined as the ratio of actual particle gasification rates (which reflect the consequences of reactive gas concentration gradients inside particles) to maximum possible particle conversion rates (which would occur if reactive gas concentrations inside particles were uniform at the levels existing at the particle periphery) for each reactive gas. The effectiveness factors are correlated with the species Thiele moduli, permitting the use of the detailed reaction mechanism for characterizing the effects of the chemical reaction in the high-temperature environments typical

of fluidized-bed and entrained-flow gasifiers and combustors without the need to perform a time-consuming, calculation-intensive, DNS to predict particle mass loss. When a distribution of particle sizes is considered, such time-consuming calculations would have to be performed for each particle size to predict overall mass loss. To circumvent the need for the DNS calculations, a char particle gasification model[10] has been developed that employs a mean particle effectiveness factor, a mode of conversion submodel[11] that governs variations in particle size and apparent density with mass loss, and a specific surface area evolution submodel that correlates specific surface area with char conversion. This approach greatly simplifies modeling gasification behavior at high particle temperatures when both particle size and apparent density vary during char conversion as a result of concentration gradients existing inside particles. The model facilitates the development of robust computational fluid dynamics (CFD) codes for prediction of the performance of advanced entrained-flow and fluidized-bed gasifiers. These CFD codes will include the fluid dynamic and heat and mass transport effects that govern gas temperatures and species concentrations at the outer surfaces of particles. The char particle gasification model permits the prediction of particle mass loss rates and off-gas composition as well as variations in the particle size and apparent density, depending upon the properties of the gaseous environment existing around the particle.

The details of the char particle gasification model, which is applicable to particles in the pulverized fuel size range as well as to larger particles in the size range appropriate for fluidized beds, were presented in a previous publication.[10] In this prior work, the heterogeneous reaction mechanism only described char reactivity to O_2 and CO_2 and a simple first-order relation was used in the determination of the effectiveness factors. These limitations are eliminated in the work presented here. In this modification of our char particle gasification model, char reactivity to H_2O is included and the effectiveness factor relations employed deviate from the first-order relations, taking into account the inhibiting effects of H_2 and CO on char gasification rates.

2. THEORETICAL DEVELOPMENT

In the intrinsic chemical reactivity model developed, the effectiveness factor (η) is used to determine the overall particle conversion rate as a result of the chemical reaction when a concentration gradient exists inside a particle. The approach of Thiele[12] is taken, wherein the effectiveness factor is related to the Thiele modulus, φ, a dimensionless parameter that gives a relative measure of the char conversion rate to the diffusion rate of reactive gas inside the particle. In our approach, a Thiele modulus is defined for each reactive gas as follows:

$$\varphi_{H_2O} = r_P\sqrt{\frac{\hat{R}_{i,H_2O,ex}\rho_C S_{gC}}{C_{H_2O,ex}D_{H_2O,eff}}} \qquad \varphi_{CO_2} = r_P\sqrt{\frac{\hat{R}_{i,CO_2,ex}\rho_C S_{gC}}{C_{CO_2,ex}D_{CO_2,eff}}}$$

$$\varphi_{O_2} = r_P\sqrt{\frac{\hat{R}_{i,O_2,ex}\rho_C S_{gC}}{C_{O_2,ex}D_{O_2,eff}}} \tag{1}$$

In the expressions, r_P is the particle radius, $\hat{R}_{i,i,ex}$ and $C_{i,ex}$ are the intrinsic chemical reactivity to species i and concentration of species i, respectively, both evaluated at the outer surface of the particle, $D_{i,eff}$ is the effective diffusion coefficient for species i through the pores of the particle, and ρ_C and S_{gC} are the apparent density and mass-specific surface area, respectively, of the char particle. Note that the Thiele moduli can be calculated without knowing the reactive gas

distributions inside the particle, only the concentrations at the outer surface of the particle.

2.1. Determination of Effectiveness Factor–Thiele Modulus Relationships. To determine the relationship between the effectiveness factor and the Thiele modulus for each reactive gas (the η_i–φ_i relationships), a DNS of a char particle exposed to reactive gas i was performed to determine the concentration gradient established inside the particle and the overall particle conversion rate consistent with the concentration gradient for selected ambient conditions (selected temperatures and reactive gas concentrations). Gas temperatures and reactive gas concentrations were varied over a range that yielded conditions in which chemical kinetics limited particle conversion rates (effectiveness factors of unity) to conditions in which the transport of reactive gas to the outer surfaces of particles limited particle conversion rates (very small values of the effectiveness factor). Because over the temperature range of interest small particles (less than about 50 μm) have kinetics-limited conversion rates and large particles (greater than about 200 μm) have diffusion-limited conversion rates, simulations were made for particles having diameters of nominally 100 μm to obtain the information needed to determine the Thiele modulus–effectiveness factor relationships. At each condition, the effectiveness factor η_i was calculated as the ratio of the overall reaction rate of reactive gas i to its maximum possible reaction rate inside the particle, with the maximum possible reaction rate being the overall reaction rate calculated assuming that the concentration of reactive gas i is uniform throughout the particle at the value existing at the outer surface of the particle.

$$\eta_i = \frac{\text{actual overall reaction rate of reactant species } i}{\text{maximum possible reaction rate of reactant species } i} = \frac{\hat{R}_i}{\hat{R}_{max,i}} \tag{2}$$

In the DNS, the differential equations that govern the transport of the reactive gases inside the char particle were simultaneously integrated, yielding the species concentration profiles inside the particle. The governing species differential equation is given below.

$$\frac{\partial C_i}{\partial t} - \frac{1}{r^2}\frac{\partial}{\partial r}\left(r^2 D_{i,eff}\frac{\partial C_i}{\partial r}\right)$$
$$= -RR_{i,hetero}(r) - RR_{i,gas\,phase}(r) + \left[\sum RR_{all}(r)\right]X_i(r) \tag{3}$$

In this equation, $D_{i,eff}$ is the effective diffusion coefficient of species i, reflecting the combined effects of Knudsen and bulk diffusion through the pores in the char, $RR_{i,hetero}$ and $RR_{i,gas\,phase}$ are overall hetero- and homogeneous reaction rates for species i, respectively, and the final term denoting the summation over all reactions, RR_{all}, both hetero- and homogeneous reactions. The left-hand side of this equation accounts for accumulation and mass transport effects, and the right-hand side accounts for chemical reaction effects, including the impact of Stefan flow (represented by the final term in the equation), the convective flux induced at the particle surface when there is mole change upon reaction. The effective diffusion coefficient is determined via eq 4, where D_i is the bulk diffusion coefficient for species i (calculated as species i diffusing into a gas mixture) and $D_{i,K,eff}$ is the effective Knudsen diffusion coefficient for species i, determined via eq 5. In eq 5, r_p is the pore radius, θ is the particle porosity, τ is the tortuosity factor (taken as 3), R is the universal gas constant, T is the temperature, and M_i is the molar mass of species i.

$$\frac{1}{D_{i,eff}} = \frac{1}{D_i} + \frac{1}{D_{i,K,eff}} \tag{4}$$

$$D_{i,K,eff} = \frac{2r_p\theta}{3\tau}\sqrt{\frac{8RT}{\pi M_i}} \tag{5}$$

The pore radius r_p is determined via eq 6, where srf is the surface roughness factor (taken as 2).

$$r_p = \frac{2srf\theta}{\rho_C S_{gC}} \tag{6}$$

Table 1. Reaction Mechanism for Carbonaceous Solids Exposed to H_2O, CO_2, and O_2[8,14]

	reaction	reaction rate (mol m^{-2} s^{-1})
R1	$2C_f + H_2O \Leftrightarrow C(OH) + C(H)$	$\hat{R}_1 = (S/N_{AV})^2\{k_{1f}[H_2O]\theta_f^2 - k_{1r}\theta_{OH}\theta_H\}$
R2	$C(OH) + C_f \Leftrightarrow C(O) + C(H)$	$\hat{R}_2 = (S/N_{AV})^2\{k_{2f}\theta_f\theta_{OH} - k_{2r}\theta_O\theta_H\}$
R3	$C(H) + C(H) \Leftrightarrow H_2 + 2C_f$	$\hat{R}_3 = (S/N_{AV})^2\{k_{3f}\theta_H^2 - k_{3r}[H_2]\theta_f^2\}$
R4	$C(O) + C_b \rightarrow CO + C_f$	$\hat{R}_4 = (S/N_{AV})k_{4f}\theta_O$
R5	$C(OH) + C_b \Leftrightarrow HCO + C_f$	$\hat{R}_5 = (S/N_{AV})\{k_{5f}\theta_{OH} - k_{5r}[HCO]\theta_f\}$
R6	$C_b + C_f + C(H) + H_2O \Leftrightarrow CH_3 + C(O) + C_f$	$\hat{R}_6 = (S/N_{AV})^2\{k_{6f}[H_2O]\theta_f\theta_H - k_{6r}[CH_3]\theta_f\theta_O\}$
R7	$C_b + C_f + C(H) + H_2 \Leftrightarrow CH_3 + 2C_f$	$\hat{R}_7 = (S/N_{AV})^2\{k_{7f}[H_2]\theta_f\theta_H - k_{7r}[CH_3]\theta_f^2\}$
R8	$C_f + C(H) + CO \rightarrow HCO + 2C_f$	$\hat{R}_8 = (S/N_{AV})^2k_{8f}[CO]\theta_f\theta_H$
R9	$C(H) + C(H) \rightarrow CH_2 + C_f$	$\hat{R}_9 = (S/N_{AV})^2k_{9f}\theta_H^2$
R10	$CO_2 + C_f \Leftrightarrow C(O) + CO$	$\hat{R}_{10} = (S/N_{AV})\{k_{10f}[CO_2]\theta_f - k_{10r}[CO]\}\theta_O\}$
R11	$C_b + CO_2 + C(O) \rightarrow 2CO + C(O)$	$\hat{R}_{11} = (S/N_{AV})k_{11f}[CO_2]\theta_O$
R12	$CO + C_f \Leftrightarrow C(CO)$	$\hat{R}_{12} = (S/N_{AV})\{k_{12f}[CO]\theta_f - k_{12r}\theta_{CO}\}$
R13	$CO + C(CO) \rightarrow CO_2 + C_f + C_b$	$\hat{R}_{13} = (S/N_{AV})k_{13f}[CO]\theta_{CO}$
R14	$2C_f + O_2 \rightarrow C(O) + CO$	$\hat{R}_{14} = (S/N_{AV})^2k_{14f}[O_2]\theta_f^2$
R15	$2C_f + O_2 \rightarrow C_2(O_2)$	$\hat{R}_{15} = (S/N_{AV})\{(S/N_{AV})k_{15f}[O_2]\theta_f^2 - k_{15r}\theta_{O_2}\}$
R16	$C_f + C_b + C(O) + O_2 \rightarrow CO_2 + C(O) + C_f$	$\hat{R}_{16} = (S/N_{AV})^2\{k_{16f}[O_2]\theta_f\theta_O - k_{16r}[CO_2]\theta_f\theta_O\}$
R17	$C_f + C_b + C(O) + O_2 \rightarrow CO + 2C(O)$	$\hat{R}_{17} = (S/N_{AV})^2k_{17f}[O_2]\theta_f\theta_O$
R18	$C_b + C_2(O_2) \rightarrow CO_2 + 2C_f$	$\hat{R}_{18} = (S/N_{AV})k_{18f}\theta_{O_2}$

Solution to the set of coupled equations formed when eq 3 is written for each species, yielding the species concentration profiles inside the particle. The $RR_{i,\text{gas phase}}$ term in eq 3 is calculated using GRI-Mech 3.0,[13] and the $RR_{i,\text{hetero}}$ term is calculated using the heterogeneous reaction mechanism presented in Table 1, along with expressions for the net reaction rates (in mol m^{-2} s^{-1}), in terms of site fractions.

This reaction mechanism, developed by Tilghman and Mitchell,[8,14] accurately describes the intrinsic chemical reactivities of several coal and biomass chars to CO_2, H_2O, and O_2. In the mechanism, $C(X_i)$ denotes an adsorbed species (i.e., a carbon site filled with an adsorbed species X_i), C_f denotes a free carbon site (i.e., a carbon site available for adsorption), and C_b denotes a bulk carbon site (an underlying site that will be exposed upon by desorption of a carbon atom from the carbonaceous matrix). The activity of a bulk carbon site is taken to be unity. The adsorbed complex $C_2(O_2)$ (see reactions R15 and R18) represents two adjacent adsorbed oxygen atoms (i.e., oxygen atoms adsorbed onto adjacent carbon sites). Whereas the adsorbed complex $C(O)$ is representative of carbonyl- and ether-type complexes that desorb to yield CO (via reaction R4), the adsorbed complex $C_2(O_2)$ is representative of lactone- and acid anhydride-type complexes that desorb to yield CO_2 (via reaction R18). In the reaction rate expressions shown in Table 1, the concentrations of gas-phase species (e.g., $[CO_2]$, $[H_2O]$, $[O_2]$, and $[H_2]$) are expressed in mol/m^3 and the forward reaction rate coefficients for reaction k (k_{kf}) are expressed in Arrhenius form: $k_{kf} = A_k \exp(-E_k/RT)$. The reverse reaction rate coefficients (k_{kr}) are calculated from the forward reaction rate coefficients and the equilibrium constant for the reaction, using the energies of formation and absolute entropies for the adsorbed species determined in the work of Tilghman and Mitchell.[8,14] In the rate expressions, the total site density for the carbonaceous matrix, S, is taken to be 6×10^{19} sites/m^2 and N_{AV} is Avogadro's number. Kinetic parameters for the chars of Wyodak coal, a sub-bituminous B coal from the Powder River Basin region of Wyoming, and corn stover, a common agricultural waste product in areas where corn is grown, have been reported[8] and are employed in this work. The mechanism and associated rate parameters accurately predict nearly all of the trends reported in the literature during coal char gasification and combustion, including high-pressure effects on char reactivity and the inhibiting effects of H_2 and CO on char reactivity to H_2O and CO_2. It also captures the observed trends in the CO/CO_2 product ratio during char combustion, yielding values within the 95% confidence range for the spread in reported values.[15]

In our approach, a spherical char particle was discretized into many concentric shells; the species conservation equations for the reactive gas and products of reaction in each shell were solved simultaneously, yielding their concentration profiles inside the particle. This permitted the calculation of reaction rates at given radii inside the particle, providing a means to determine the actual overall particle gasification rate. The ratio of the actual overall particle conversion rate to the maximum possible conversion rate (the rate evaluated using the reactive gas concentrations at the outer surface of the particle, where they are maximum) yields the effectiveness factor. With the effectiveness factor determined, the contributions of internal and external gasification rates to the overall particle gasification rate can be evaluated as a function of the temperature for specified particle sizes without the need to perform a time-consuming, calculation-intensive, DNS.

Each of the concentric shells into which the spherical particle is divided represents a volume element that contains an initial mass of material, determined from the initial apparent density of the char. Taking the true density of the carbonaceous material to be 2000 kg/m^3, the porosity of each volume element can be calculated and, thus, so can a value for its mean pore radius (via eq 6). The species concentrations in each shell are then solved for numerically, with the boundary conditions being the surface concentrations determined by balancing the overall consumption of each gas with the flux of the gases from the bulk of the particle to the outer surface of the particle.

It should be noted that, as a result of the distributions of reactive gases within the particle (and associated distribution in char conversion rate), porosity and pore radius begin to differ for each shell as gasification progresses and so does the effective diffusion coefficient for each shell. Also, the outermost shell will have the highest conversion rate because the reactive gas concentrations are highest at the particle periphery. When the extent of conversion in the outermost shell is greater than 99%, we assume that the particle radius decreases an amount equal to the thickness of this outer shell. In effect, the DNS will predict the variations in the particle size and apparent density as gasification progresses. This was demonstrated in our previous work.[11]

Shown in Figure 1 are calculated variations in diameter, for both Wyodak coal and corn stover char particles, during gasification in an ambient of pure CO_2 at 1 atm and a range of temperatures. The calculations were made assuming an initial particle diameter of 100 μm. When the CO_2 concentration is uniform inside particles, conversion occurs throughout particle volumes; the apparent densities of the particles decrease with mass loss, while changes in diameters are negligible. Such is the case at 1000 °C, the normalized radius ($r_s/r_{s,0}$) remains near unity until the late stages of char conversion. For both chars, gasification rates at 1000 °C (and lower temperatures) are in the so-called zone I gasification regime, the regime in which the rates of
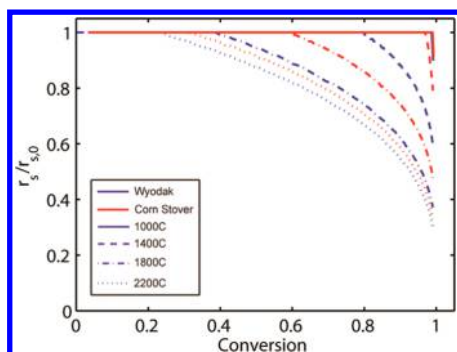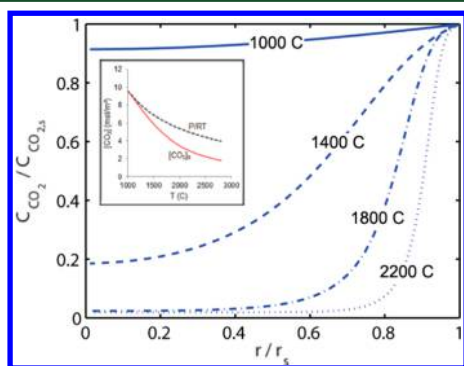
Figure 1. Normalized particle radius as a function of char conversion.

chemical reactions control the overall char conversion rates. At 1400 °C, a decrease in diameter is noted at about 80% conversion for the Wyodak coal char, indicative of concentration gradients inside the coal char particle. At 1400 °C, the reactivity of the coal char has increased to the extent that chemical reactions are beginning to consume CO_2 before it can completely penetrate the particle. Coal char reaction rates are even higher at 1800 °C and still higher at 2200 °C, causing the penetration depth of CO_2 to become less and less until, at higher temperatures, the CO_2 is completely consumed at the periphery of the char particle. When this occurs, the char particles are said to gasify in the zone III regime, in which CO_2 diffusion to the outer surfaces of char particles limit their overall gasification rates. At temperatures between 1400 and 2200 °C, the Wyodak coal char particles gasify in the zone II regime, the regime in which the combined effects of chemical reaction and pore diffusion limit overall gasification rates.

The behavior is the same with the corn stover char particles, but because these char particles have a higher porosity than the coal char particles and, hence, are easier to penetrate, higher temperatures (faster reaction rates) are needed before CO_2 penetration is significantly limited. As noted in Figure 1, at temperatures as high as 1800 °C, the diameters of the biomass char particles do not start to change until over 60% conversion. At 2200 °C, the corn stover char particles have gasification rates that fall into the zone II regime.

Shown in Figure 2 are the calculated normalized concentration profiles for the Wyodak coal char particles. As noted, at 1000 °C, the


Figure 2. Normalized CO_2 concentration versus normalized particle radius for Wyodak coal char particles exposed to 100% CO_2 at various temperatures. The CO_2 concentration at the outer particle surface as a function of the temperature is shown in the inset.

CO_2 concentration profile is nearly uniform inside the particles, indicative of gasification in the zone I regime. At 1400 °C, a gradient exists in the CO_2 profile but reaction rates are not quite high enough to prevent CO_2 from reaching the center of the particle. At 1800 °C, reaction rates are sufficiently high to prevent CO_2 from reaching the center of the particle, and at 2200 °C, the CO_2 concentration profile is quite steep, falling to less than 10% of its value at the outer surface at only 20% of the radial distance from the wall. The concentration gradients established at temperatures between 1400 and 2200 °C are

indicative of gasification in the zone II regime. As illustrated in the inset of Figure 2, the CO_2 concentration at the outer surface of the particle decreases with an increasing particle temperature. When temperatures are high enough to render the CO_2 concentration at the outer surface to nearly zero, gasification is in the zone III regime, the regime in which overall particle conversion rates are limited by the transport of reactive gases to the outer surface of the particle, and the conversion rates are diffusion-limited.

The DNS results provided the means to determine the actual overall particle gasification rate at the specified ambient condition, from which the effectiveness factor was determined. To determine the effectiveness factor−Thiele modulus relationship, the full numerical simulation was executed over a range of temperatures and gas concentrations. During the course of each simulation, the Thiele modulus and effectiveness factor were calculated and stored. It should be noted that, for specified reactor conditions, both the Thiele modulus and effectiveness factor vary with the extent of conversion, because the particles become more porous with mass loss, and this impacts mass transport. These two parameters are then plotted against each other, so that a relationship can be determined.

Shown in the left panel of Figure 3 are $\eta_i - \varphi_i$ relationships determined from several DNSs of Wyodak coal and corn stover char
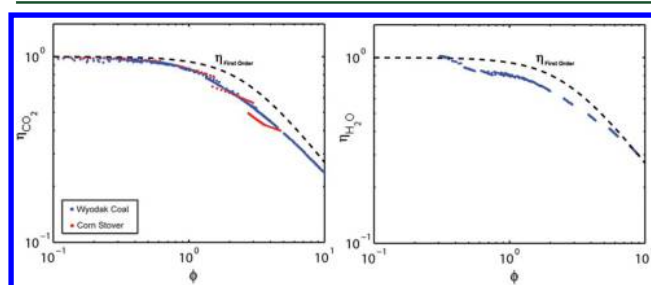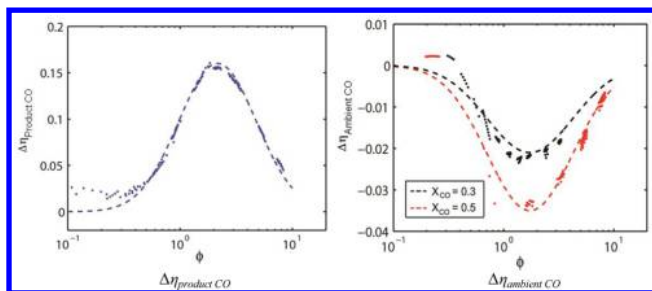

Figure 3. Effectiveness factor as a function of the Thiele modulus for Wyodak coal and corn stover char particles exposed to CO_2 over a range of temperatures up to 2200 °C (left) and for Wyodak coal char particles exposed to H_2O at selected temperatures up to 2200 °C (right).

particles exposed to 100% CO_2 over a range of temperatures up to 2200 °C. At low temperatures, the concentration profiles inside the particle are uniform and η_{CO_2} is near unity. As temperature increases, concentration gradients inside the particles progressively steepen and η_{CO_2} progressively decreases. For very small values of η_{CO_2}, chemical reaction is confined primarily to the periphery of the particle; overall particle conversion rates become diffusion-limited.

The dashed line in the left panel of Figure 3 represents the theoretical relation derived by Thiele[12] for steady-state, first-order, irreversible reaction in a sphere. As noted, in 100% CO_2, the char−CO_2 reaction mechanism exhibits near first-order behavior. We attribute the deviations from first-order behavior to inhibition by CO, via the reverse of reaction R10 or reactions R12 and R13. If the ambient gas contains even modest levels of CO, the $\eta−\varphi$ relationship is altered further, because this affects the internal CO gradients that arise from the carbon gasification (and also changes the reactivity at the surface, thus changing the comparison between the reactivity of internal shells to that at the surface).

Shown in the right panel of Figure 3 are $\eta_i−\varphi_i$ relationships determined from several DNSs of Wyodak coal char particles exposed to H_2O over a range of temperatures up to 2200 °C. Deviations from the first-order relationship ($\Delta\eta$) are primarily due to inhibition by H_2, which is formed in reaction R3. The DNS results were analyzed to determine the deviations from first-order behavior as a result of CO and H_2 as products of the heterogeneous reactions and CO and H_2 as part of the ambient gas.

Shown in Figure 4 are results obtained for $\Delta\eta$ for the char−CO_2 reaction mechanism, and shown in Figure 5 are the results obtained for the char−H_2O reaction mechanism, where $\Delta\eta$ signifies the difference

Figure 4. Deviations in the effectiveness factor from first-order behavior as a result of CO as a heterogeneous reaction product (left) and CO in the ambient gas (right) for the char–CO_2 heterogeneous reaction mechanism. In both panels, the dashed lines represent Gaussian fits to the calculated differences.
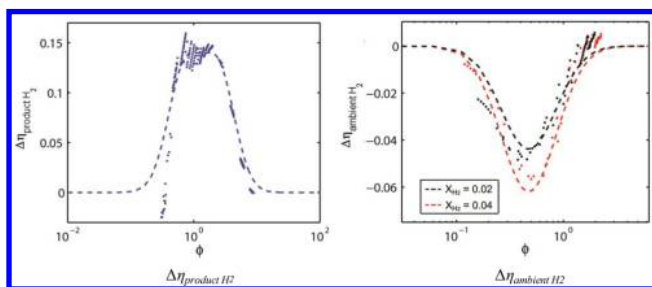
Figure 5. Deviations in the effectiveness factor from first-order behavior as a result of H_2 as a heterogeneous reaction product (left) and H_2 in the ambient gas (right) for the char–H_2O heterogeneous reaction mechanism. In both panels, the dashed lines represent Gaussian fits to the calculated differences.

between the actual effectiveness factor and the first-order predicted effectiveness factor. To obtain the information needed to evaluate these differences, the DNS model was run several times, varying the temperature over a range of values for different $CO_2/CO/N_2$ mixtures and different $H_2O/H_2/N_2$ mixtures. The deviations exhibit a Gaussian shape and, thus, were empirically correlated with φ via the Gaussian expressions below (eqs 7–10). The deviation shape for the "product H_2" was not quite close enough to a Gaussian shape as a result of its wider peak but was well fit by the sum of two identical Gaussian curves with different means.

$$\Delta\eta_{\text{product CO}} = 0.16 \exp\left(\frac{-(\ln(\varphi) - 0.77)^2}{2(0.8)^2}\right) \qquad (7)$$

$$\Delta\eta_{\text{ambient CO}} = -(0.07)X_{\text{CO}} \exp\left(\frac{-(\ln(\varphi) - 0.55)^2}{2(0.9)^2}\right) \qquad (8)$$

$$\Delta\eta_{\text{product H}_2} = \sum_{\mu_i} 0.12 \exp\left(\frac{-(\ln(\varphi) - \mu_i)^2}{2(0.6)^2}\right) \qquad \mu_1 = 0.9,$$

$$\mu_2 = -0.35 \qquad (9)$$

$$\Delta\eta_{\text{ambient H}_2} = -(0.32)\sqrt{X_{\text{H}_2}} \exp\left(\frac{-(\ln(\varphi) + 0.75)^2}{2(0.6)^2}\right) \qquad (10)$$

A deep investigation into the explanation for the shape of these effectiveness factor deviations is beyond the scope of this paper. However, in general, it is likely that, at relatively low Thiele moduli, inhibition does not impact the effectiveness factor because internal gradients of the inhibiting gases are negligible. At relatively high values for Thiele moduli (which typically corresponds to relatively high temperatures or reactivities), the inhibitory nature of CO and H_2 is reduced, often attributed to the reduced residence times of surface species. Between these values, when there are internal gradients of

inhibitory gases as well as a temperature that is appropriate for the gases to indeed inhibit reactivity, the deviation from first-order Thiele modulus–effectiveness factor behavior is most evident. This also offers a potential explanation for the flatter peak of the "product H_2" deviation, which requires two Gaussian curves to fit. It has been posited by many researchers that H_2 can inhibit carbon reactivity in two ways: by adsorbed C(H) species occupying reactive sites and by adsorbed or gaseous hydrogen reacting with adsorbed C(O) species before they get a chance to desorb as gaseous CO. Both of these modes are accounted for in this mechanism. Each mode may have a different Thiele modulus at which its contribution to first-order-deviation peaks, and overall behavior is an overlap of these two modes. Another explanation is that one of these peaks is attributable to internal inhibition by CO, which is also a product of H_2O gasification. Indeed, one of the Gaussian curves involved in the fit for product H_2 is very similar to that for product CO.

Note that the deviations associated with CO and H_2 in the ambient gas depend upon their mole fractions (X_i) in the ambient gas mixture. With these deviations, the η_i–φ_i relationships for the char–CO_2 and char–H_2O heterogeneous reaction mechanisms are given as follows:

$$\eta_{\text{CO}_2}(\varphi) = \eta_{\text{1st order}}(\varphi) - \Delta\eta_{\text{product CO}}(\varphi) - \Delta\eta_{\text{ambient CO}}(\varphi) \qquad (11)$$

$$\eta_{\text{H}_2\text{O}}(\varphi) = \eta_{\text{1st order}}(\varphi) - \Delta\eta_{\text{product H}_2\text{O}}(\varphi) - \Delta\eta_{\text{ambient H}_2\text{O}}(\varphi) \qquad (12)$$

where the first-order relationship is given by

$$\eta_{\text{1st order}} = \frac{3}{\varphi}\left(\frac{1}{\tanh(\varphi)} - \frac{1}{\varphi}\right) \qquad (13)$$

This expression was derived by Thiele[12] for a spherical particle undergoing reaction at steady state, assuming a one-step, irreversible char consumption reaction.

As evidenced by the agreement demonstrated in Figure 6, eqs 7–13 yield satisfactory predictions of the η_i–φ_i relationships for the char–
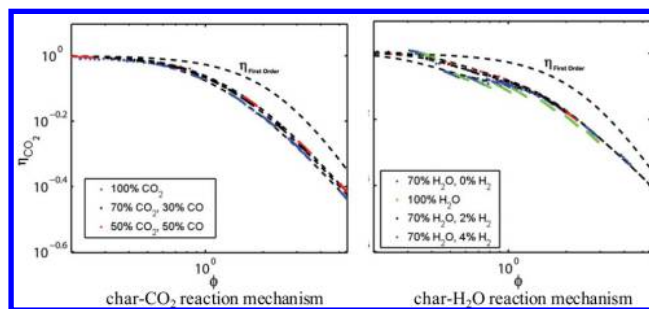
Figure 6. Effectiveness factor–Thiele moduli relationships determined from the DNSs (points) and calculated from eqs 7–13 (solid and dashed lines) for the char–CO_2 (left) and char–H_2O (right) heterogeneous reaction mechanisms.

CO_2 and char–H_2O heterogeneous reaction mechanisms (dashed lines in the figures). It should be noted that the scatter in the DNS results are due to the fact that the η_i–φ_i relationships were obtained throughout the course of char conversion, even before steady-state concentration profiles were established inside the particle. Most of the scatter is associated with determining η during these periods. In most of the simulations, steady-state concentration profiles were not attained until over 50% char conversion.

The above equations permit the accurate determination of overall char particle conversion rates in the environment containing CO_2 and H_2O at high temperatures. Because char reactivity to O_2 is so much faster than char reactivity to H_2O and CO_2 and the key oxidation reactions are essentially irreversible, the η_{O_2}–φ_{O_2} relationship for the char reaction in environments containing oxygen were found to be well-predicted by Thiele's first-order formulation (eq 13). Thus

$$\eta_{O_2}(\varphi) = \frac{3}{\varphi}\left(\frac{1}{\tanh(\varphi)} - \frac{1}{\varphi}\right) \tag{14}$$

The actual overall reaction rate of all reactive gases is given as follows in terms of the species-specific effectiveness factors:

$$\hat{R} = \sum_{i=1}^{N_{\text{reactants}}} \hat{R}_i = \sum_{i=1}^{N_{\text{reactants}}} \eta_i \hat{R}_{\text{max},i} \tag{15}$$

The reaction rates of the individual species were determined from the reaction mechanism presented in Table 1. The maximum possible overall reaction of all reactive gases is given by

$$\hat{R}_{\text{max}} = \sum_{i=1}^{N_{\text{reactants}}} \hat{R}_{\text{max},i} \tag{16}$$

With these equations employed, besides the species-specific effectiveness factors given by eq 2, a mean effectiveness factor for the particle is also defined.

$$\eta = \frac{\text{actual overall reaction rate of all reactant species}}{\text{maximum possible reaction rate of all reactant species}}$$

$$= \frac{\hat{R}}{\hat{R}_{\text{max}}} \tag{17}$$

The mean effectiveness factor is a key parameter in the char particle gasification model, as indicated in the following sections.

2.2. Char Particle Mode of Conversion Relations. The char particle gasification model includes a mode of conversion submodel,[11] in which the effectiveness factor governs how the apparent density of the carbonaceous portion of a char particle and its size vary as mass is lost as a result of the heterogeneous reaction. In the mode of conversion submodel, the mass of a char particle (m_p) changes owing to the changes in the mass of the carbonaceous particle material (m_C) during gasification and is followed in time by integrating the following equation:

$$\frac{dm_p}{dt} = \frac{dm_C}{dt} = -\eta R_C S_g m_C \tag{18}$$

Here, R_C is the carbon reactivity (g m^{-2} s^{-1}), evaluated employing the reaction mechanism presented in Table 1 and the concentrations of the reactive species and temperature at the outer surface of the particle. When the apparent density of the carbonaceous material in the very thin outermost shell at the periphery of the particle falls to zero, the particle diameter will start to decrease. As demonstrated in our previous work,[11] this occurs at the time when char conversion (x) equals the time-averaged effectiveness factor $\bar{\eta}$. For $x < \bar{\eta}$, the radius of the particle is constant ($r_p = r_{p0}$, where r_{p0} is the initial particle radius), while the apparent density of the carbonaceous particle material is decreasing, such that $\rho_C = \rho_{C0}(m_C/m_{C0})$. For $x > \bar{\eta}$, the radius and apparent density of the carbonaceous material decrease; the smaller the effectiveness factor, the more the fractional change in the radius. For very small values of $\bar{\eta}$, the apparent density of the carbonaceous material remains essentially constant during conversion. The following piecewise power-law relations are used to reflect this conversion mode as mass loss progresses in time:

$$\frac{\rho_{C,t+dt}}{\rho_{C,t}} = \begin{cases} \left(\dfrac{m_{C,t+dt}}{m_{C,t}}\right) & \text{if } x \le \bar{\eta} \\[3mm] \left(\dfrac{m_{C,t+dt}}{m_{C,t}}\right)^{\eta} & \text{if } x > \bar{\eta} \end{cases} \tag{19}$$

$$\frac{r_{p,t+dt}}{r_{p,t}} = \begin{cases} 1 & \text{if } x \le \bar{\eta} \\[3mm] \left(\dfrac{m_{C,t+dt}}{m_{C,t}}\right)^{1-\eta/3} & \text{if } x > \bar{\eta} \end{cases} \tag{20}$$

With knowledge of the char particle mass, radius, and apparent density at time t, eq 18 is integrated to determine the mass of the carbonaceous material at time $t + dt$ and eqs 19 and 20 are used to determine the apparent density of the carbonaceous material and particle radius at the new time. The following expression is used to determine the mass specific surface area of the carbonaceous particle material at the new time:

$$S_{\text{gC},t+dt} = S_{\text{gC},0}\sqrt{1 - \psi \ln(1 - \rho_{C,t+dt}/\rho_{C,0})} \tag{21}$$

Here, ψ is a structural parameter that depends upon the structure of the pore network within the carbonaceous material. This expression is based on the work of Bhatia and Perlmutter[16] and is consistent with their work for char conversion in the zone I regime, in which the apparent density ratio equals char conversion (i.e., in zone I, at any time, $\rho_{C,t}/\rho_{C,0} = x$). For Wyodak coal char, ψ equals 8, and for corn stover char, ψ equals 7, based on the work of Mitchell.[14] With these values for ψ, the mass specific surface area increases with decreases in the apparent density of the char during char conversion.

The equations were tested in simulations, and model predictions were compared to predicted results of a full DNS. The goal of the mode of conversion submodel is to predict results consistent with the predictions of the DNSs.
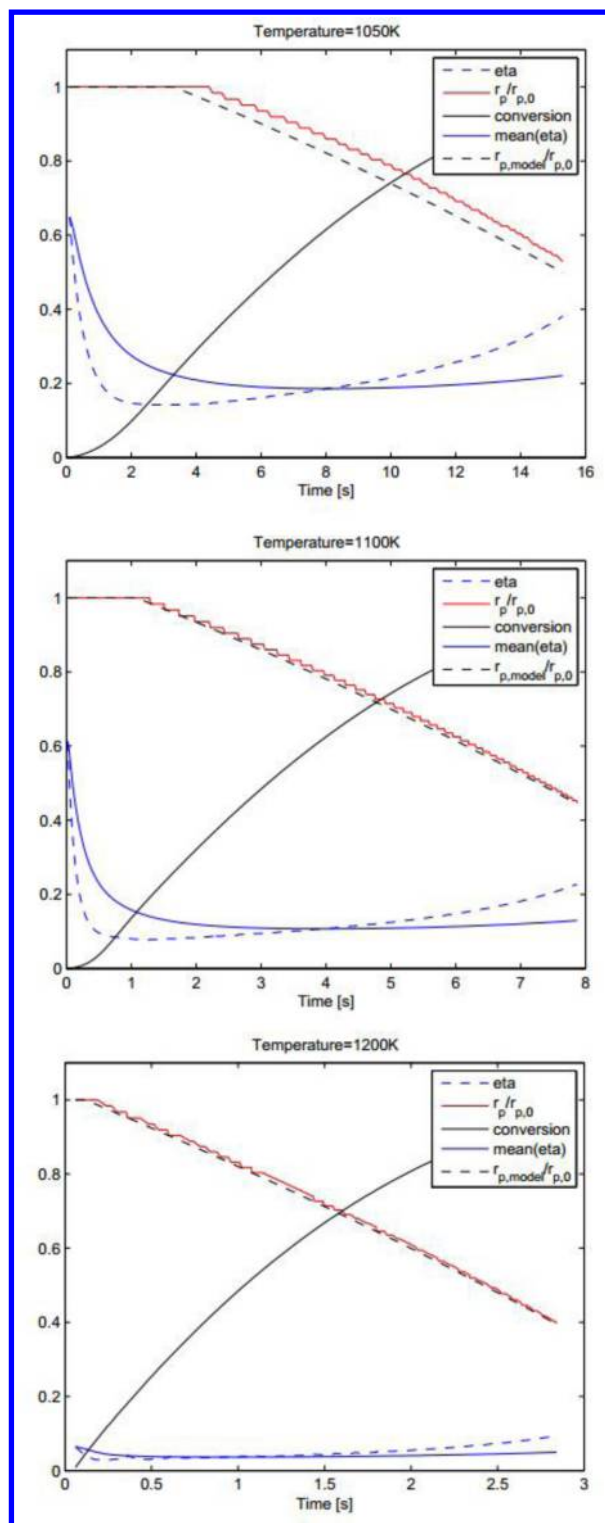
Comparisons of predicted size profiles for a 100 μm diameter char particle exposed to 6% oxygen, by volume, at selected temperatures indicate excellent agreement, as evidenced in Figure 7. Calculations were made employing the kinetic parameters for the reactivity of Wyodak coal char. Shown in the figure are variations in particle normalized radius, mean effectiveness factor, and conversion as time progresses. Owing to the significantly higher conversion rates in oxygen, the rapid changes in the morphology of the particle provide a stringent test of the model. As noted in the figure, similar to the DNS code, the mode of conversion submodel predicts that the particle radius starts to decrease at earlier times (and at earlier conversions) as the temperature is increased. The agreement depicted serves to validate the use of eqs 19 and 20 to predict changes in the char particle size and apparent density with mass loss.

The temporal variations in the mean value of the effectiveness factor (see Figure 7) are noted to exhibit a rapid decrease at early extents of conversion, with a more uniform variation at higher conversions as steady-state conditions are approached. The higher the temperature, the more rapid the decrease in the effectiveness factor from its initial value. The scatter exhibited in the plots shown in Figures 3−6 is due to values of the effectiveness factor determined during these rapid transients at early stages of conversion.

2.3. Char Particle Gasification Model. The char particle gasification model combines all of the submodels discussed into a single model capable of predicting char particle behavior in environments of specified temperature, pressure, and composition. It uses the heterogeneous reaction mechanism for char reactivity to H_2O, CO_2, and O_2 put forth in Table 1, along with the Thiele modulus−effectiveness factor relationships (eqs 7−17), the mode of conversion submodel (eqs 18−20), and the specific surface area evolution submodel (eq 21). Multi-species diffusion across the boundary layer surrounding the particle is taken into account, as described in our previous work,[10] when evaluating the Thiele moduli. The model also takes into account heat transfer effects, which include the energy released and absorbed as a result of chemical reactions (Q_{reac}), combined conduction and convection between the particle and its surrounding gas (Q_{con}), and radiation from the particle (Q_{rad}). The energy conservation equation is expressed as follows:

$$m_p c_{p,p} \frac{dT_p}{dt} = Q_{\text{reac}} + Q_{\text{con}} + Q_{\text{rad}} \tag{22}$$

where T_p, m_p, and $c_{p,p}$ are the temperature, mass, and specific heat, respectively, of the particle. Expressions for Q_{rad} can be found in our previous work.[17] When Q_{reac} is evaluated, the thermochemical data needed to calculate the heats of reaction of the heterogeneous reactions listed in Table 1 were taken from the work of Tilghman and Mitchell.[8,14] An account is made for Stefan flow when determining the

Figure 7. Comparison of predicted particle size profiles as a function of the char conversion and time for an initially 100 μm diameter particle exposed to 6% oxygen at selected temperatures: mode of conversion model (black dashed line) and DNS model (red solid line). Effectiveness factor and time-averaged effectiveness factor predicted by the mode of conversion model are also shown (blue dashed line and blue line, respectively).

combined heat transfer coefficient between the particle and gas when evaluating Q_{con} and for particle-to-wall radiation exchange as well as for particle-to-particle radiation exchange when evaluating Q_{rad}. When Q_{rad} is evaluated, the particle can be assumed to be near the center of a

cloud of similar reacting particles where particle-to-particle radiation exchange is dominant, near the periphery of a cloud of particles where particle-to-wall radiation is significant, or somewhere in between where both particle-to-particle and particle-to-wall radiation exchange play significant roles in cooling gasifying char particles.

The energy equation is integrated simultaneously with eq 18 to yield the particle mass and temperature as char conversion progresses. Input conditions include a description of the gaseous environment to which the particle is exposed and the initial properties of the char particle, in particular the initial particle size, apparent density, specific surface area, temperature, and ash content.

2.4. Accounting for Ash in the Particle. In the model, the ash is assumed to consist of discrete small particles that are distributed uniformly throughout the volume of the particle. The ash is also assumed to have insignificant influence on the behavior of the particle during mass loss. Whether or not an ash film is formed at the particle periphery or whether ash components soften or melt and diffuse into the carbonaceous matrix, an ash dilution effect[18] is outside the scope of the present model. In essence, it is assumed that the ash is inert, remains with the particle during mass loss, and poses no limitations to the transport of reactive gases to the carbonaceous particle material.

The mass of the char particle at any time equals the mass of the ash plus the mass of the carbonaceous material that has not yet been gasified ($m_p = m_{ash} + m_C$). Assuming that no ash leaves the particle during the gasification process, the apparent density of the ash-containing particle (ρ_p) at a time when the mass of the particle is m_p can be determined via the following expression:

$$\frac{1}{\rho_p} = \frac{X_{ash}}{\rho_{ash}} + \frac{(1 - X_{ash})}{\rho_C}$$

$$= \frac{X_{ash,0}}{(m_p/m_{p,0})\rho_{ash}} + \frac{(1 - X_{ash,0}/(m_p/m_{p,0}))}{\rho_C} \quad (23)$$

where X_{ash} and ρ_{ash} are the instantaneous mass fraction and apparent density, respectively, of the ash in the particle and the subscript "0" denotes initial values. The mass of the particle at any time (m_p) is determined via integration of eq 18, and the corresponding apparent density of the carbonaceous material in the particle (ρ_C) is determined via eq 19. The apparent density of the ash is taken to be constant at 2300 kg/m³, a value consistent with the values determined from the specific gravities of fly ashes and bottom ashes found in coal-fired utility boilers.[19] The finely divided ash is assumed to be distributed within the carbonaceous matrix, clinging to pore walls. Any ash clinging to the outside of a char particle is assumed to be in the sub-micrometer-to-micrometer size range, sufficiently small so as not to contribute to the overall size of the char particle. No buildup of an ash layer surrounding the particle is assumed to occur during mass loss. Consequently, eq 20 applies to the ash-containing particle.

The mass specific surface area of the ash-containing char particle ($S_{g,p}$) is assumed to include contributions from both the ash and the carbonaceous material and is expressed as follows:

$$S_{g,p} = X_{ash}S_{g,ash} + (1 - X_{ash})S_{gC} \quad (24)$$

The specific surface area of the ash is taken to be in the range of 5−10 m²/g, the range of the values measured in our laboratory for several samples of coal ash, and the instantaneous specific surface area of the carbonaceous material is determined via eq 21. For most coal and biomass chars, the mass specific surface area of the char particle is dominated by the mass specific surface area of the carbonaceous material within the particle.

Similarly, the instantaneous specific heat of the char particle is assumed to include contributions from both the ash and the carbonaceous particle material and is expressed as

$$c_{p,p} = X_{ash}c_{p,ash} + (1 - X_{ash})c_{p,C} \quad (25)$$

Such an approach is consistent with the formulations of Merrick[20] for estimating the thermal properties of coals. The specific heat of the ash and the specific heat of the char, which depend upon its elemental

composition, are calculated via the correlations put forth by Merrick.[20] In the above equations, the instantaneous fraction of ash in the particle (X_{ash}) and the fraction of the particle mass remaining ($m_p/m_{p,0}$) are calculated from the extent of char conversion (x) via the following relations:

$$X_{ash} = 1/(1 + (1 - x)(1 - X_{ash,0})/X_{ash,0}) \quad (26)$$

$$m_p/m_{p,0} = (1 - X_{ash,0})(1 - x) + X_{ash,0} \quad (27)$$

3. RESULTS AND DISCUSSION

To demonstrate the capability of the particle gasification model, it was used to assess the contributions that various effects have on overall particle behavior during gasification. In the calculations that follow, a cloud of 100 μm diameter Wyodak coal char particles of specified number density was assumed to be exposed to an environment typical of that established in an oxygen-blown entrained-flow gasifier operating at 24 bar and 1640 K. The carbon/gas mass ratio inside the enclosure was taken to be 0.65, and the gaseous environment was assumed to consist of 73% O_2, 14% N_2, and 13% H_2O, initially, i.e., before injection of any coal char. The initial particle temperature was taken as 1500 K, a consequence of devolatilization (a process not included in the gasification model). GRI-Mech 3.0[13] was used to describe the effects of the homogeneous reaction in the gas phase. Ash-free particles are assumed in the calculations that follow, with emphasis being placed on the behavior of the reactive portion of the particle material.

In the left-hand panel of Figure 8, char conversion is shown as a function of time for different cases, with the black line
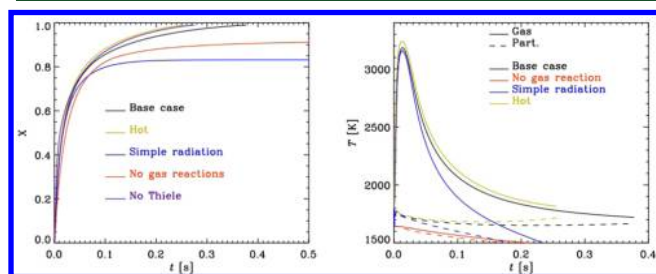
Figure 8. Char particle conversion (left) and particle and gas temperatures (right) calculated for a 100 μm diameter char particle in a cloud of particles ($mass_{carbon}/mass_{gas}$ = 0.65) exposed to a gaseous environment containing 73% O_2, 12% H_2O, and 14% N_2 (by volume) at 24 bar and 1640 K, initially.

being the base case where all processes are taken into account. The initial increase in conversion is very fast because the carbonaceous material is consumed via reactions with oxygen. The conversion rate slows at about 75% conversion as oxygen is consumed, and steam becomes the dominant gasification agent. For the base case, about 78% of the total time used to reach full conversion is spent gasifying only the last 20% of the particle mass.

In the right-hand panel of Figure 8, the particle and gas-phase temperatures are shown as a function of time. The high gas-phase temperature in the vicinity of the particles at early times is due to gas-phase reactions, as seen by comparing the base case and the case without gas-phase reactions (red line). Hydrogen and carbon monoxide that leave the particle surface are oxidized, providing the energy to drive the endothermic steam gasification reactions. The gas-phase temperature falls from its peak value of over 3000 K to around 1800 K at the end

of the gasification process. The particle temperature increases to about 1800 K at the time the gas temperature peaks and falls to only about 1650 K before complete conversion. As evidenced in the figure, if it were not for the energy release as a result of the homogeneous reaction, char particle temperatures would be low (as a result of less convective heat transfer from the gas) and char conversion would not reach 100% before heterogeneous reactions become frozen, owing to the low particle temperatures.

If account is not made for the concentration gradients established inside the particle (a consequence of fast reaction rates relative to pore diffusion rates inside the particle) and the species concentration profiles are assumed to be uniform, the particle conversion rate is too high, as evidence by the case labeled "no Thiele", and the particle reaches full conversion in a shorter time than for the base case. The gas and particle temperatures also exceed their base case values if proper account is not made for the reduced overall conversion rate when the reactive gases do not totally penetrate the porous char particle.

In traditional approaches to modeling radiation losses from char particles, only radiation exchange between the particle and the enclosure walls is taken into account (simple radiation case, blue line). Because this traditional approach does not take into account particle heating via radiation from all of the surrounding particles (as in the base case), it yields a particle cooling rate that is too high. The temperature evolutions for the two cases are very similar at early times, but at later times, the traditional approach (blue line) shows the effect of the stronger cooling. The cooling is actually so strong that full conversion is not reached, and the chemical reactions are quenched as a result of the low temperatures.

For the base case calculations, the char particle is assumed to be an "average" particle in the cloud of particles, a particle not near the center nor near the periphery of the cloud but somewhere in between, surrounded by radiating particles. If the particle were at the center of the cloud, its temperature would be somewhat higher than that for the base case because radiant energy loss from the particle would be minimum because the radiant energy exchange would be primarily between the particle and other hot particles, with little if any direct radiant energy exchange with the cooler enclosure walls. If the particle were near the periphery of the cloud, its temperature would be somewhat lower than that for the base case because a significant portion of the radiant energy exchange would be between the particle and the cooler walls. A more detailed discussion of the importance of interparticle radiation for pulverized solid fuel combustion is provided in our previous work[17] that focuses on this topic.

Increasing the initial gas and particle temperatures by 200 K gives a somewhat reduced gasification time, as noted from the case labeled "hot" (yellow/green line) in Figure 8. Even though both the gas and particle temperatures were initially 200 K higher than for the base case, for nearly all of the time spent gasifying the particle, the temperature difference between the two cases is less than 50 K.

To further demonstrate the utility of the particle gasification model, it was used to provide information needed to compare the conversion behaviors of Wyodak coal and corn stover char particles. Temperature profiles predicted at early times for a 100 μm diameter char particle in an enclosure that initially contains 1% O_2, 20% H_2O, and 20% CO_2 (with the balance being N_2) at 800 °C and 1 atm are shown in Figure 9 when
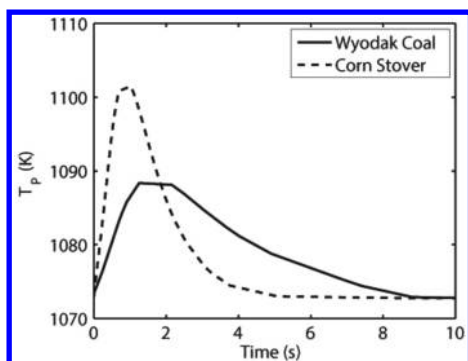
Figure 9. Early time char particle temperature profiles in an enclosure that initially contains 1% O_2, 20% H_2O, and 20% CO_2 at 800 °C and 1 atm for Wyodak coal and corn stover char particles.

kinetic parameters for Wyodak coal and corn stover chars are employed. A temperature of 800 °C is a typical gasification temperature for agricultural waste biomass, because such biomass has several considerations that require it to be gasified at a lower temperature than coal (namely, a larger ash content with a lower ash fusion temperature and a higher tendency to agglomerate).[21] The same temperature was used for the coal simulation to enable a straightforward comparison between the coal and biomass chars as well as because the moderate temperature of 800 °C allows for better investigation of the inhibition differences, which diminish at higher temperatures. As noted, the corn stover char particle attains a slightly higher peak temperature than the Wyodak coal char particle and reacts faster with oxygen as the reactive gas, reaching the peak temperature in less than half the time. These temperature profiles are during the early stages of char conversion, during the time that the char–O_2 reaction is dominant. After depletion of the oxygen, the endothermic char–H_2O and char–CO_2 reactions are responsible for char gasification, which results in a decrease in the particle temperature as char conversion progresses.

Normalized particle mass profiles for the Wyodak coal and corn stover char particles are shown in Figure 10. Neither of the
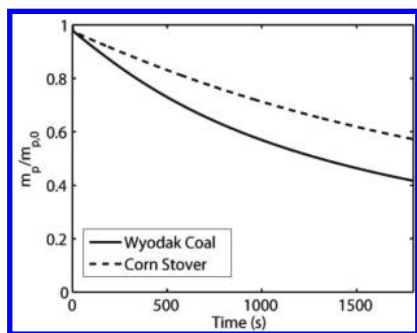

Figure 10. Char normalized mass versus time for char particles exposed to an environment that initially contains 1% O_2, 20% H_2O, and 20% CO_2 at 800 °C and 1 atm for Wyodak coal and corn stover char particles.

char particles is completely consumed in the 1800 s of simulation time in the conditions selected. During 1800 s of reaction, the coal char loses only about 60% of its initial mass and the corn stover char loses only about 40% of its initial mass, and in each case, a significant portion of the mass is lost quite early when O_2 is the primary reactant. The char conversion

rates during reactions with H_2O and CO_2 are quite low at temperatures less than 1000 °C (1273 K). As suggested in the discussion below, the reasons for such low gasification rates are due, in part, to the inhibiting effects of H_2 and CO on char reactivity to H_2O and CO_2, which become more significant as the concentrations of H_2 and CO buildup inside the enclosure. The corn stover char particles appear to be more impacted by inhibition than the Wyodak coal char particles.

The buildup of CO and H_2 in the enclosure as it is released from the char is shown in Figure 11 at early times, during
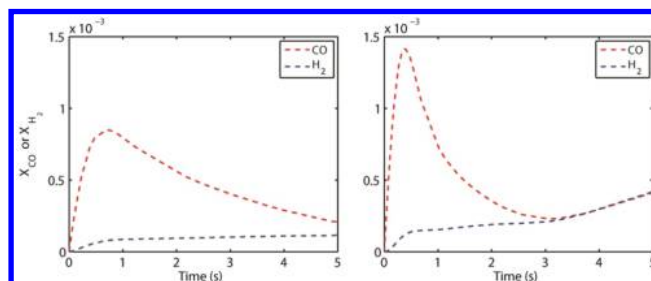
Figure 11. Production of H_2 and CO at early times in an enclosure that initially contains 1% O_2, 20% H_2O, and 20% CO_2 at 800 °C and 1 atm for Wyodak coal char particles (left) and corn stover char particles (right).
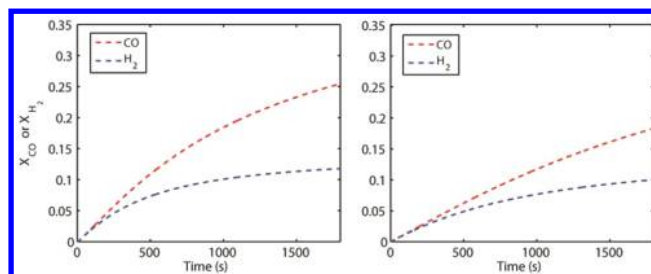
Figure 12. Production of H_2 and CO at late times in an enclosure that initially contains 1% O_2, 20% H_2O, and 20% CO_2 at 800 °C and 1 atm for Wyodak coal char particles (left) and corn stover char particles (right).

oxygen depletion, and in Figure 12 at later times when char gasification via reactions with H_2O and CO_2 controls the char conversion process. The different behaviors of the coal and the biomass chars at early times (Figure 11) are attributed predominantly to the differences in reactivity to oxygen. As already noted, the corn stover char is much more reactive to O_2 than is the Wyodak coal char, leading to an earlier and more abrupt spike in CO (a main byproduct of reaction with O_2 at these temperatures). The spike is higher not only due to intrinsic chemical differences (i.e., different rates for the reactions that produce CO versus those that produce CO_2) but also because the faster reaction with O_2 leads to higher corn stover char particle temperatures (see Figure 9). These higher temperatures lead to more CO being produced during reaction with O_2, instead of CO_2.

The spike in CO also drops quicker for the corn stover char than for the Wyodak coal char. This is somewhat surprising if one assumes that the gas-phase reaction with the remaining O_2 is predominantly responsible for the depletion of CO and the gas-phase kinetics do not differ. However, there are other factors at work. First of all, consider that, with corn stover, the

enclosure is hotter as a result of the more rapid release of energy, meaning higher gas-phase reaction rates when corn stover is the fuel. However, also important is a phenomenon related to one of the modes of inhibition for CO. One of the most important modes of inhibition by CO is the reverse of the reaction R10. When the gaseous CO molecule reacts with an adsorbed $C(O)$ complex to yield a gaseous CO_2, it prevents the $C(O)$ molecule from removing carbon from the substrate by a subsequent CO desorption. Any difference in this mode of inhibition for the two fuels is extra-evident in this scenario, where there are high amounts of $C(O)$ on the surface (as a result of the reaction in O_2) and relatively low amounts of CO_2, leading to a scenario which favors the reverse of the reaction over the forward reaction (in normal dry gasification conditions, the forward direction of the reaction is typically far faster). Indeed, for the kinetic parameters used in this work, corn stover char has a much higher reaction rate coefficient for the reverse direction of reaction R10 than the Wyodak coal char (at this temperature), about 0.10 versus 0.04 m^3 mol^{-1} s^{-1}.[8] This difference is also contributing to the quicker depletion of CO in the corn-stover-fueled enclosure. One can also see a kink upward in the production of H_2, coincident with the minimum in the CO concentration. This coincides with the depletion of ambient O_2, which consumes both H_2 and CO via gas-phase reactions.

Note that, just after oxygen depletion, for each char, the production rates of CO and H_2 are comparable, suggesting that the char−H_2O reaction (which produce CO and H_2 in nearly equal amounts) is faster than the char−CO_2 reaction (which produces only CO) at early times. As time progresses, the production rate of CO outpaces that of H_2, suggesting a decrease in the rate of the char−H_2O reaction. This is especially true for the corn stover char. The decrease in the char conversion rate is due to the inhibiting effects of H_2 and CO on char reactivity. Inhibition of H_2O gasification can occur by the reverse of reactions R1, R2, or R3. The reverse of reaction R2 eliminates $C(O)$ complexes, whose desorption into gaseous CO is the primary source of reactivity. The reverse of reaction R1 eliminates $C(OH)$ complexes, thereby reducing the number that dissociates into $C(O)$ + $C(H)$. The reverse of reaction R3 increases the number of $C(H)$ complexes, which reduces the number of free sites but also increases the reverse rates of both reactions R1 and R2. The most prominent difference between the corn stover and Wyodak coal chars at this temperature is the reverse rate of reaction R1. The rate constant for the reverse reaction of R1 (k_{1r}) for the corn stover char is over 300 times greater than it is for the Wyodak coal char.[8] The accumulation of H_2 within the enclosure increases the amount of $C(H)$ on the surface, which consequently increases the reverse rate of reaction R1, thereby reducing the net reaction rate of R1 more for the corn stover char than for the Wyodak coal char. As the concentrations of these species increase in the enclosure, the inhibiting effects increase, slowing the overall char conversion rates. Simulations performed at a higher enclosure wall temperature, 1100 °C, yielded similar results. These calculations demonstrate the use of the char particle gasification model to compare char particle conversion behavior of different fuels and at elevated temperatures.

These investigations support the use of the char particle gasification model to describe char particle conversion behavior in high-temperature environments containing CO_2, H_2O, and O_2. The model can be used to predict the fates of char particles in fluidized-bed and entrained-flow gasifiers and combustors.

The model is even applicable to oxy-combustion conditions. To accurately predict gas composition (for instance, the mole fractions of CO, H_2, CO_2, H_2O, CH_4, and O_2 within the gasifier or combustor), the char particle gasification model must be combined with a detailed homogeneous reaction mechanism that characterizes CH_4 formation (such as GRI-Mech 3.0[13]).

4. CONCLUSION

The reactant-specific effectiveness factor−Thiele modulus relations presented in this paper provide a means of using a heterogeneous reaction mechanism developed at low temperatures, when chemical kinetics govern char conversion rates, to be used at high temperatures, when the combined effects of chemical kinetics and pore diffusion govern overall char particle conversion rates. In combination with the mode of conversion and mass specific surface area submodels, these relations permit the prediction of the variations in char particle size, apparent density, and temperature during char conversion in environments of specified initial temperature, pressure, and composition. Model predictions agree with observations, suggesting that the char particle gasification model can be used as a tool to provide a fundamental understanding of the processes governing char conversion behavior during gasification and combustion. The model is applicable to all char particle sizes undergoing mass loss in any conversion regime, either the zone I, II, or III conversion regime.

■ AUTHOR INFORMATION

Corresponding Author
*Telephone: 650-725-2015. E-mail: remitche@stanford.edu.
ORCID ⊙
Reginald E. Mitchell: 0000-0002-0510-5018
Notes
The authors declare no competing financial interest.

■ REFERENCES

(1) Charpenay, S.; Serio, M. A.; Solomon, P. A. *Symp. Combust., [Proc.]* **1992**, *24*, 1189−1197.
(2) Salatino, P.; Senneca, O.; Masi, S. *Carbon* **1998**, *36* (4), 443−452.
(3) Liu, G.-S.; Tate, A. G.; Bryant, G. W.; Wall, T. F. *Fuel* **2000**, *79* (10), 1145−1154.
(4) Hla, S. S.; Harris, D. J.; Roberts, D. G. CFD Modeling for an Entrained Flow Gasification Reactor Using Measured "Intrinsic" Kinetic Data. *Proceedings of the 5th International Conference on CFD in the Process Industries*; Melbourne, Australia, Dec 13−15, 2006.
(5) Seo, D. K.; Lee, S. K.; Kang, M. W.; Hwang, J.; Yu, T.-U. *Biomass Bioenergy* **2010**, *34* (12), 1946−1953.
(6) Mani, T.; Mahinpey, N.; Murugan, P. *Chem. Eng. Sci.* **2011**, *66* (1), 36−41.

(7) Hecht, E. S.; Shaddix, C. R.; Geier, M.; Molina, A.; Haynes, B. S. *Combust. Flame* **2012**, *159*, 3437−3447.

(8) Tilghman, M. B.; Mitchell, R. E. *Combust. Flame* **2015**, *162* (9), 3220−3235.

(9) Mitchell, R. E.; Ma, L.; Kim, B.-J. *Combust. Flame* **2007**, *151*, 426−436.

(10) Haugen, N. E. L.; Mitchell, R. E.; Tilghman, M. B. *Combust. Flame* **2015**, *162* (4), 1455−1463.

(11) Haugen, N. E. L.; Tilghman, M. B.; Mitchell, R. E. *Combust. Flame* **2014**, *161* (2), 612−619.

(12) Thiele, E. W. *Ind. Eng. Chem.* **1939**, *31* (7), 916−920.

(13) Smith, G. P.; Golden, D. M.; Frenklach, M.; Moriarty, N. W.; Eiteneer, B.; Goldenberg, M.; Bowman, C. T.; Hanson, R. K.; Song, S.; Gardiner, W. C., Jr.; Lissianski, V. V.; Qin, Z. *GRI-Mech 3.0*; http://www.me.berkeley.edu/gri_mech/version3.0.

(14) Mitchell, R. E. *Gasification Characteristics of Coal/Biomass Mixed Fuels*; National Energy Technology Laboratory (NETL), United States Department of Energy (U.S. DOE): Morgantown, WV, Sept 2014; Award DE-FC26-10FE0005372.

(15) Campbell, P. A.; Mitchell, R. E. *Combust. Flame* **2008**, *154* (1−2), 47−66.

(16) Bhatia, S. K.; Perlmutter, D. D. *AIChE J.* **1980**, *26* (3), 379−386.

(17) Haugen, N. E. L.; Mitchell, R. E. *Heat Mass Transfer* **2015**, *51* (7), 991−999.

(18) Lunden, M. M.; Yang, N. Y. C.; Headley, T. K.; Shaddix, C. R. *Symp. Combust., [Proc.]* **1998**, *27*, 1695−1702.

(19) Electric Power Research Institute (EPRI). *Coal Ash: Characteristics, Management and Environmental Issues*; EPRI: Palo Alto, CA, Sept 2009.

(20) Merrick, D. *Fuel* **1983**, *62*, 540−546.

(21) Devi, L.; Ptasinski, K. J.; Janssen, F. J. J. G. *Biomass Bioenergy* **2003**, *24*, 125−140.